Experimental Thermal and Fluid Science 101 (2019) 16–26

Contents lists available at ScienceDirect

Experimental Thermal and Fluid Science

journal homepage: www.elsevier.com/locate/etfs

Assessment of film cooling's surface quantities using pressure- and temperature-sensitive paint: Comparisons between shaped and sand-dune inspired holes

Wenwu Zhou[a,b], Di Peng[a,b], Yingzheng Liu[a,b,*], Hui Hu[c]

[a] Key Lab of Education Ministry for Power Machinery and Engineering, School of Mechanical Engineering, Shanghai Jiao Tong University, 800 Dongchuan Road, Shanghai 200240, China
[b] Gas Turbine Research Institute, Shanghai Jiao Tong University, 800 Dongchuan Road, Shanghai 200240, China
[c] Department of Aerospace Engineering, Iowa State University, 2271 Howe Hall, Room 1200, Ames, IA 50011, USA

ARTICLE INFO

Keywords:
Film cooling
PSP and TSP
Barchan dune
Adiabatic effectiveness
Heat transfer coefficient
Net heat flux reduction

ABSTRACT

Following the previous work (Zhou and Hu, 2017), a comprehensive assessment was performed to further evaluate the film cooling's surface quantities behind shaped and sand dune-inspired holes. Adiabatic film cooling effectiveness, heat transfer coefficient, and net heat flux reduction (NHFR) were measured at four blowing ratios (M = 0.40, 0.90, 1.40, and 2.00). The measured quantities were compared side-by-side between the shaped and sand dune-inspired holes. The pressure-sensitive paint (PSP) technique was used to acquire high-resolution adiabatic effectiveness and the temperature-sensitive paint (TSP) technique was used to map the corresponding heat transfer coefficient over the surface. Nitrogen and air, with a density ratio of about one, were used as the coolant for the PSP and TSP tests respectively. The measured results showed that the adiabatic effectiveness of the Barchan dune-shaped injection compound (BDSIC) was significantly higher than that of the shaped hole. Improvements of 20–150% in the centerline and 30–400% in the laterally averaged effectiveness were observed behind the BDSIC compared to the shaped hole. As for the heat transfer performance, although the BDSIC showed 10–20% higher heat transfer coefficient, h_f/h_0, the measured spatially averaged NHFR still demonstrated an augmentation of 50–150% in heat flux reduction in comparison to the shaped hole. This paper represents the first effort to comprehensively evaluate the surface quantities behind BDSIC film cooling concept using both PSP and TSP techniques.

1. Introduction

In modern gas turbines, the film cooling technique has been extensively used to isolate vital components from extremely hot gas. Featured as a jet-in-cross-flow configuration, the cooling air is bled through the coolant hole to form a thin coolant blanket over the protected surface [2–4]. Given the challenge of improving film cooling performance at reduced levels of coolant consumption, considerable efforts have been made to optimize the cooling hole's geometries [5–8] to ensure stable coverage of the coolant film over the influential area. In recent times, the appearance of additive manufacturing technique has further inspired novel film cooling hole concepts, such as the anti-vortex hole [9,10], the dumbbell-shaped hole [11], the sweeping jet [12], and sand dune-inspired concepts [1,13]. Substantial investigations have shown superior cooling performance for new cooling holes than the conventional circular hole, especially for the sand dune-inspired concepts [1], which was inspired by the unique shape of sand dunes in deserts. The proposed Barchan dune-shaped injection compound (BDSIC) [1] had demonstrated significant improvement in cooling effectiveness (i.e., 30–500%) and reduced loss at high blowing ratios compared to the circular hole. But, detailed PIV results also demonstrated a complex vortex dynamic behind the dune, which is dramatically different from that of the shaped hole. The complex vortices would lead to complicated spatial distributions of surface cooling quantities. These quantities, which are closely associated with thermal stress, are regarded as important parameters in the community of structural integrity analysis. However, no heat transfer results have been reported yet. Therefore, it is highly desirable to quantify the surface cooling quantities behind the BDSIC in a comprehensive manner, including adiabatic effectiveness, heat transfer coefficient, and

* Corresponding author at: Key Lab of Education Ministry for Power Machinery and Engineering, School of Mechanical Engineering, Shanghai Jiao Tong University, 800 Dongchuan Road, Shanghai 200240, China.
E-mail address: yzliu@sjtu.edu.cn (Y. Liu).

https://doi.org/10.1016/j.expthermflusci.2018.10.005
Received 15 April 2018; Received in revised form 5 October 2018; Accepted 5 October 2018
Available online 06 October 2018
0894-1777/

Nomenclature

Bi	Biot number
D	diameter of coolant injection hole
D_s	concentration diffusion coefficient
DR	coolant-to-mainstream density ratio, ρ_c/ρ_∞
h_f	heat transfer coefficient with film cooling
h_0	heat transfer coefficient without film cooling
h_i	heat transfer coefficient of internal cooling
I	coolant-to-mainstream momentum ratio, $\rho_c U_c^2/\rho_\infty U_\infty^2$
Le	Lewis number,α/D_s
M	blowing ratio or mass flux ratio, $\rho_c U_c/\rho_\infty U_\infty$
MW	molecular weight ratio of coolant to mainstream
$(p_{o_2})_{air}$	partial pressure of oxygen with air as the coolant
$(p_{o_2})_{mix}$	partial pressure of oxygen with non-oxygen gas as the coolant
Pr	Prandtl number
q_w''	net local heat flux
Re	Reynolds number
T_{aw}	adiabatic wall temperature
T_c	coolant stream temperature
T_∞	mainstream flow temperature
U_c	coolant stream velocity
U_∞	incoming flow velocity
VR	velocity ratio, U_c/U_∞
x_0	unheated starting length

Greek symbols

α	thermal diffusion coefficient
θ	injection angle
δ_{99}	boundary layer thickness
δ^{**}	momentum thickness
η	instantaneous film cooling effectiveness
φ	non-dimensional metal temperature

Abbreviations

BDSIC	barchan dune-shaped injection compound
CRV	counter-rotating vortex
NHFR	net heat flux reduction
PSP	pressure-sensitive paint
TSP	temperature-sensitive paint

net heat flux reduction (NHFR).

Numerous techniques have been applied to map the spatial distributions of surface cooling quantities over protected surfaces. Aside from the traditional thermocouples used in earlier studies, advanced optical-based techniques, such as liquid crystal thermometry [14], infrared thermometry [15], pressure-sensitive paint (PSP) [16], and temperature-sensitive paint (TSP) [17], have been widely used in recent times. The measurement of cooling quantities can generally be classified into temperature-based and mass transfer-based methods. The temperature-based methods have been widely used to determine the film effectiveness and heat transfer performance. Using infrared thermometry, Baldauf et al. [15,18] separately analyzed film cooling coefficient and heat transfer performance behind a circular hole. Narzary et al. [17] applied the TSP technique to study the coolant density effect on film cooling effectiveness. A similar method was adopted by Russin et al. [19], who measured the heat transfer of a circular hole. Compared to "hot" experiments, mass transfer-based methods (such as the naphthalene sublimation and PSP techniques), which can eliminate the concern of heat conduction loss, are also popular methods. Chen and Goldstein [20] used naphthalene sublimation for simulating the heat transfer on a blade. Haring et al. [21] simulated heat transfer on a turbine blade airfoil. As for the PSP technique, Wright et al. [22] studied the effect of the density ratio (DR) on film effectiveness using PSP. Khojasteh et al. [23] used PSP for successfully resolving the effectiveness patterns near a coolant hole. It is worth noting that Russin et al. [19], who combined both the PSP and TSP techniques, successfully measured the film cooling effectiveness, heat transfer performance, and NHFR. This strategy offers an alternative solution for obtaining surface quantities in a comprehensive manner but with reduced complexity in the experimental system - without the requirement for heating up the mainstream flow. Therefore, a complementary PSP and TSP measurement was conducted in this study.

We extensively evaluated the surface quantities of film cooling behind the shaped and BDSIC holes. It was assessed in terms of adiabatic film effectiveness (η), heat transfer coefficient (h), and NHFR. The shaped hole was treated as the baseline due to its wide application in gas turbines. This paper represents the first effort to comprehensively quantify the thermal performances behind BDSIC, which aren't included in the previous paper [1]. The PSP technique was used to acquire adiabatic effectiveness and the TSP technique was used to map the corresponding heat transfer over the surface. Based on the acquired effectiveness and heat transfer results, high-resolution NHFR was computed for all the tested cases. This study is expected to help us further evaluate the potential of implementing the BDSIC in engine cooling. Note that, previous experiments [1] for BDSIC used carbon dioxide as the coolant. But, Nitrogen is used in the present study (for the PSP tests) to ensure the same density ratio (i.e., $DR \approx 1.0$) with that of the heat transfer experiments (i.e., TSP tests). In general, this paper attempts to quantify the surface cooling quantities rather than flow quantities [1] for a better understanding of the overall cooling performance of BDSIC.

2. Experimental apparatus and measurement techniques

2.1. Experimental models and test conditions

In this study, all film cooling models were constructed layer by layer using a 3D printing machine that has a resolution of 50 μm. Fig. 1 shows the schematic configuration of the shaped and BDSIC test models. Note that, the shaped hole is a reproduction of the previously designed 7-7-7 shaped hole [24], which opens 7° in lateral directions and 7° laidback toward the surface. But the injection angle is 35° for the present study rather than 30° in the reported 7-7-7. The shaped hole consists of a 2.8D long cylindrical tube and a 2.2D diffused section. The diameter of the circular part is 8 mm. Fig. 1(b) illustrated the proposed BDSIC concept, which is the same as that in the literature [1]. It features with a 2.9D wide and 4.3D long dune shell that could cover the circular hole completely. Based on the alignment holes on the surface, the hollow dune was attached to the circular hole using 80-μm thick double-sided tape. All test models were polished carefully to achieve desired surface quality with 2000-grit sandpaper. The test plate was flush against the bottom wall to avoid potential misalignments. A relatively large plenum with dimensions of 150 mm × 200 mm × 180 mm was mounted below the flat plate and would be able to provide stable coolant flow.

The film cooling and heat transfer experiments were performed in a low speed, suction-type wind tunnel located at Shanghai Jiao Tong University. The tunnel has a 320 mm × 80 mm optically transparent test section with a corresponding hydraulic diameter, D_h, of 128 mm. To achieve low-turbulent uniform flow, honeycombs and fine screens were placed ahead of tunnel contraction. The flow inside the test section was

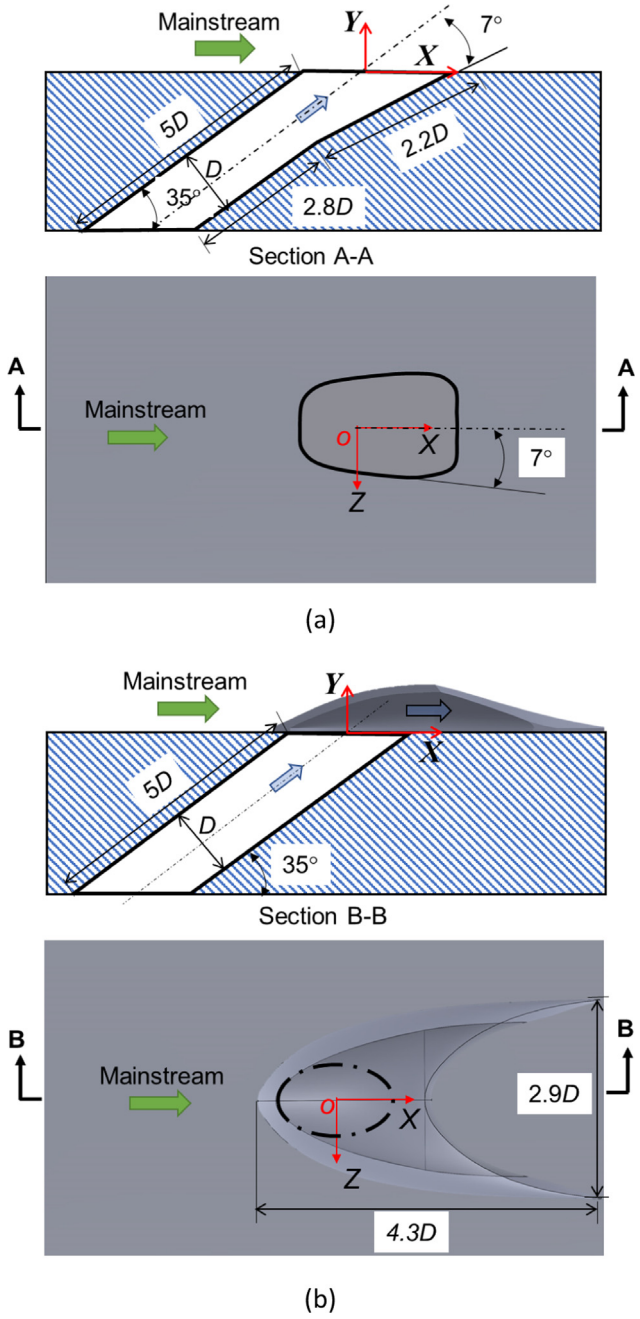

Fig. 1. The schematic of the (a) shaped hole and (b) BDSIC hole, where D is the diameter of coolant hole.

found to be around 1.1% as measured by hot-wire anemometer. Mainstream airflow and nitrogen (i.e., density ratio of 0.98) were used to simulate the hot gas and coolant flow for the PSP tests, respectively. However, to match density ratio, pure air was selected as the coolant for the TSP experiments. The coolant gas, supplied by a pressurized gas cylinder (99.99% purity), passed through a long pipeline and constant-temperature thermal bath to reach an equivalent temperature with the mainstream before injecting into plenum. A flowmeter (Omega, FMA-1610A) was chosen to monitor the blowing ratios (i.e., $M = \rho_c U_c/\rho_\infty U_\infty$). In this study, the blowing ratio was varied from 0.40 to 2.00 to successively simulate jet attaching, partially, and fully taking-off. Its corresponding momentum ratio ($I = \rho_c U_c^2/\rho_\infty U_\infty^2$) and velocity ratios ($V_r = U_c/U_\infty$) was varied from 0.16 to 4.08 and from 0.41 to 2.04, respectively. The incoming flow was maintained constant at 9.1 m/s, and the corresponding Reynolds number was about 4850 with respect to the hole diameter (i.e., 8 mm). The freestream boundary layer was developed at approximately 50D ahead before reaching the leading edge of the coolant hole. The velocity profile was measured by a hot-wire probe (Dantec, 55P11-16). It was confirmed to be fully developed and had a boundary layer thickness of $\delta_{99} \approx 1.4D$ and momentum thickness of $\delta^{**} \approx 0.12D$. During the experiment, the uncertainty level of flowmeter reading was less than 1%. And the measured velocity uncertainty was estimated to be within 3%.

2.2. Measuring the adiabatic film cooling effectiveness using the pressure-sensitive paint technique

As an important dimensionless parameter, the adiabatic film cooling effectiveness is normalized by adiabatic wall temperature T_{aw} and defined as:

$$\eta = \frac{T_\infty - T_{aw}}{T_\infty - T_c} \tag{1}$$

An effectiveness values of $\eta = 1.0$ represents a perfect coolant coverage on the surface, while that of $\eta = 0$ denotes no coolant protection. As mentioned above, varieties of techniques have been used to determine the film cooling effectiveness. In the present study, we utilized the pressure-sensitive paint to quantify the effectiveness distribution. It is a method that uses mass transfer analogy to simulate heat transfer process. With the Lewis number ($Le = \alpha/D_s$) around 1.0, the thermal and concentration boundary layer is of the same thickness, denoting a heat and mass transfer analogy within the two differential equations [25,26]. Since PSP experiments are performed under isothermal condition, the heat conduction errors associated with the temperature-based method can be eliminated easily. Based on mass transfer analogy, the adiabatic effectiveness Eq. (1) can be further expressed as Eq. (2) [27], where MW is the coolant-to-mainstream molecular weight ratio.

$$\eta = 1 - \frac{1}{[((p_{o_2})_{air}/(p_{o_2})_{mix})_{wall} - 1]MW + 1} \tag{2}$$

When the PSP coated surface is illuminated by certain ultraviolet lights, it will emit certain photoluminescence that has longer wavelengths than the light source. However, the excited molecules may return to the ground state via reduced or radiation-less emission with the appearance of diatomic oxygen molecules. This is the so-called oxygen quenching process. Furthermore, the photoluminescence intensity is inversely proportional to the local oxygen concentration. Therefore, based on recorded light intensity and calibration process [23], the adiabatic effectiveness can be calculated through application of Eq. (2). Further technical details of pressure-sensitive paint technique and calibration procedures can refer to the literature of Wright et al. [22] and Zhou and Hu [13].

Noted that, comparative studies were performed by Zhou and Hu [13] and Johnson et al. [16] to quantify the differences between PSP measurements and those obtained from temperature-based methods. Good agreement was reported within these techniques. Applying similar experimental setups to those used in Zhou and Hu [13], the PSP technique was utilized to map the effectiveness distributions at various blowing ratios.

Fig. 2(a) shows the experimental setup for the PSP experiments. A high-power ultraviolet LED light (UHPT-LED-385, Prizmatix) with a wavelength of 385 nm was used as the excitation source. A high-resolution CCD camera (PCO1600, Cooke Corp.) was used to record the photoluminescence at a sampling rate of 3 Hz. A 650 nm ± 50 nm band-pass filter mounted ahead of the camera was used to filter out background noise from the ambient environment. The experimental study was conducted in isothermal conditions with a constant environmental temperature of 21 °C ± 0.5 °C. The PSP images were recorded at 0.06 mm per pixel, resulting in a spatial resolution of 0.03D. The measurement uncertainty of the PSP experiment was estimated to

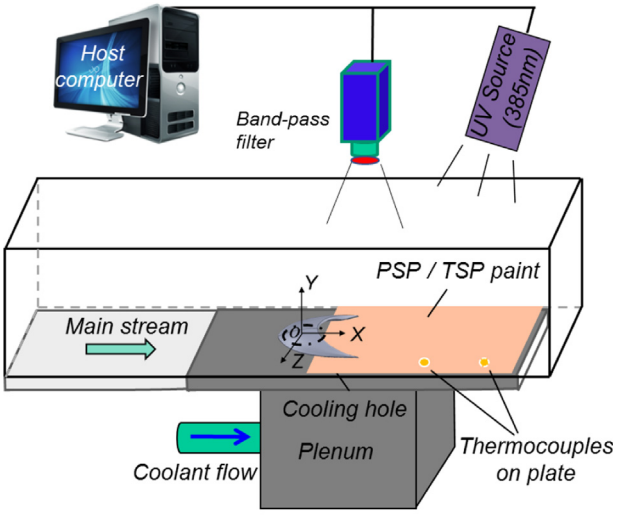

(a) PSP and TSP experimental setup

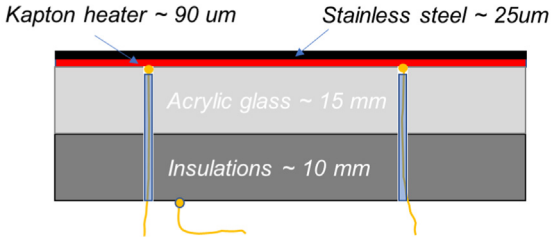

(b) Constant heat flux setup for TSP

Fig. 2. Experimental setups for the PSP and TSP measurements.

be within 5% for $\eta \geqslant 0.4$. The uncertainty level was determined by the PSP calibration, the quality of the acquired images, and the flow conditions of the incoming flow and coolant streams [16].

2.3. Measuring the heat transfer coefficient using the temperature-sensitive paint technique

The heat transfer coefficients (h_f) [8,28] for film cooling were measured using the TSP technique, which is defined as follows:

$$h_f = \frac{q''_w}{T_w - T_\infty} = \frac{q''_{gen} - q''_{loss}}{T_w - T_{aw}} \tag{3}$$

where q_w'' is the net local heat flux, q_{gen}'' is the generated heat flux from the heater, and q_{loss}'' is the local heat loss due to heat conduction and radiation. The parameter T_w is the steady-state local wall temperature when the heater is on, and T_{aw} is the adiabatic wall temperature measured with the incoming airflow on but the heating element off (i.e., approximately equal to the mainstream temperature). Two parallel tests were performed separately to obtain the final heat transfer coefficients (h_f). First, the adiabatic wall temperature (T_{aw}) was measured with the heater off but wind tunnel on. The heater was then turned on and the local wall temperature (T_w) was measured once the system reached steady state. Consequently, h_f could be easily computed based on the measured results from both tests. In this study, the mainstream and coolant air were maintained at room temperature, but the test plate was heated up by an ultra-thin heater that could be treated as a constant flux condition. Further information about the heat transfer theory of film cooling can be found in the literature [8,29–31].

The main purpose of film cooling is to isolate the excessive heat from the mainstream and protect the hot-section components in the gas turbine. As a result, the overall performance of film cooling should be evaluated in terms of NHFR, which considers both film cooling and heat transfer from the hot gas to the protected surface.

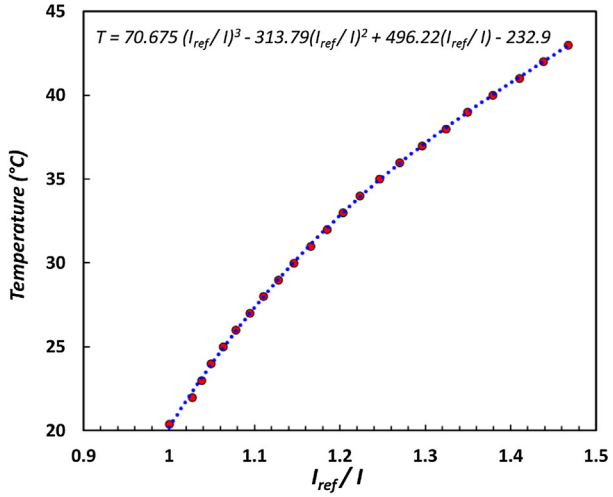

(a) TSP Calibration curve

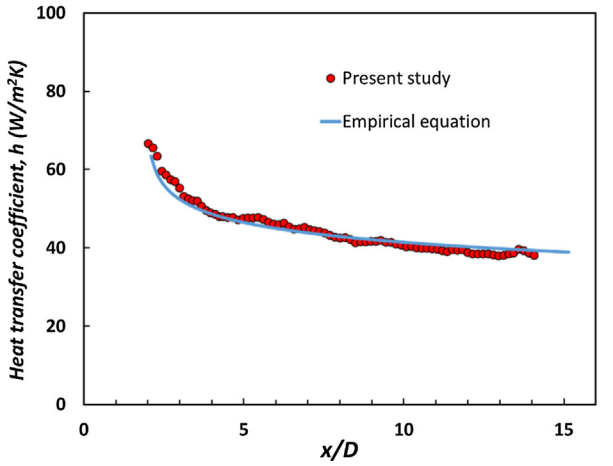

(b) Measured values vs predictions from empirical equation [32]

Fig. 3. TSP calibration curve and verification of measured heat transfer coefficient by using TSP technique.

$$h_0 = \frac{q''_{0gen} - q''_{0loss}}{T_w - T_\infty} \tag{4}$$

$$NHFR = 1 - \frac{h_f}{h_0}\left(1 - \frac{\eta}{\varphi}\right) \tag{5}$$

$$\varphi = \frac{1-\eta}{1 + Bi + h_f/h_i} + \eta \text{ [32]} \tag{6}$$

where h_0 is the heat transfer coefficient for the case without coolant injection (i.e., flat plate results were used in this study), q_{0gen}'' and q_{0loss}'' are the corresponding heat flux and local heat loss, respectively, φ is the non-dimensional metal temperature, Bi is the Biot number (ht/k, where t is airfoil thickness, and k is the thermal conductivity), and h_f/h_i is the ratio of the external heat transfer coefficient to the internal heat transfer coefficient. As noted by Johnson et al. [32], Bi and h_f/h_i were estimated as $Bi = 0.35$ and $h_f/h_i = 3.1$ for a typical engine condition. Consequently, the NHFR distributions behind coolant holes can be obtained if the values of both η and h_f/h_0 are known. It should be noted that one limitation of this strategy lies in the deviation of density ratio from typical values for film-cooled turbine vanes and blades, which usually in the range of 1.5–2.0 [4,33]. This limitation might lead to

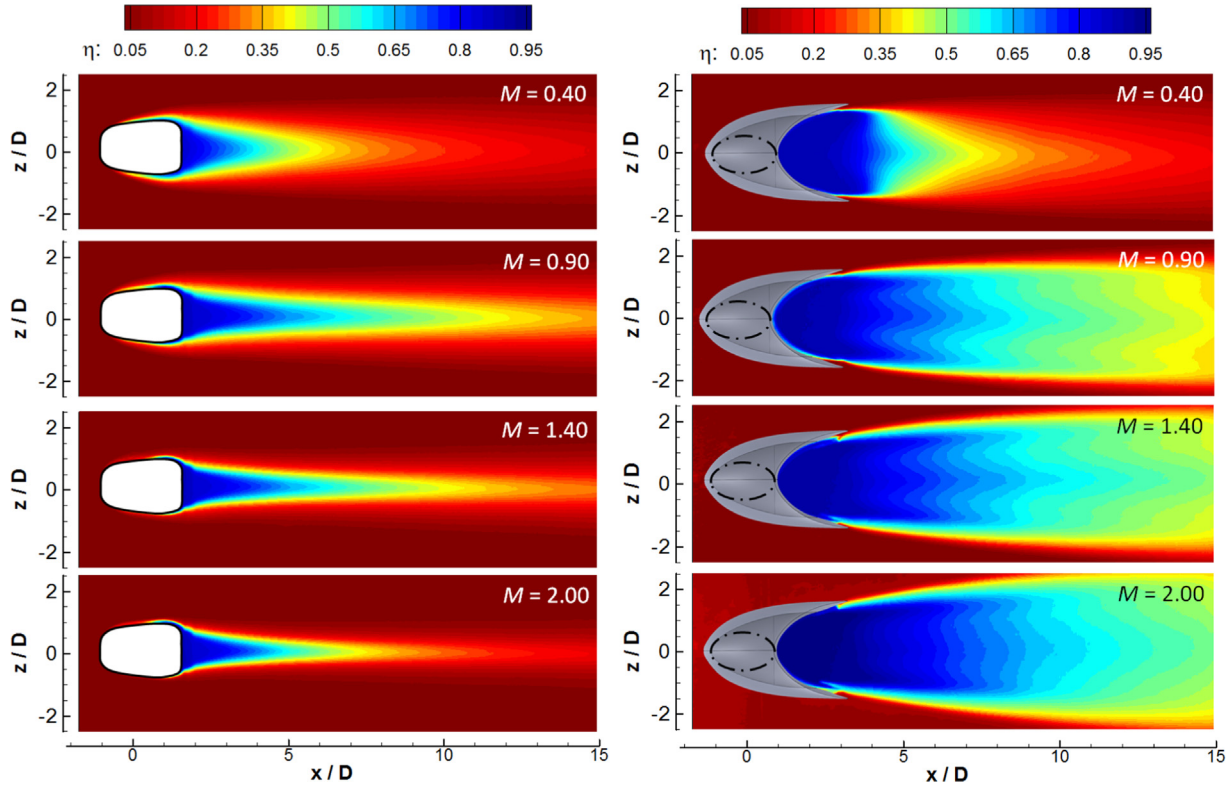

Fig. 4. Measured film cooling effectiveness distributions for the shaped hole and the BDSIC designs at various blowing ratios.

different cooling performance over the protected surface since the corresponding momentum ratio would be overestimated if the blowing ratio was fixed but with a lighter coolant (i.e., DR ≈ 1.0).

In this study, the TSP technique was utilized to quantify the heat transfer coefficient behind the shaped and BDSIC holes. The test surface was coated with layers of TSP, consisting of luminescent molecules that emit luminance when illuminated by certain wavelengths of light. Excited TSP molecules may also return to the ground state without light emission via a thermal deactivation process, namely the so-called thermal quenching process [34,35]. This process is inversely proportional to the local surface temperature. As the surface temperature rises, the quantity of thermally deactivated molecules increases but the luminescence intensity decreases.

The experimental setup for TSP is similar to that of the PSP. It shared the same LED light source but was equipped with a different band-pass filter (600 nm). Furthermore, the same camera with the exact same configuration was used in this test to map the temperature field. This ensured that the heat transfer distributions would exactly match with the film effectiveness fields. Several thermocouples were welded on the top surface to monitor the surface temperature and perform the TSP calibration. As for the multi-layer heat flux configuration (Fig. 2 (b)), an ultra-thin Kapton heater (~90 μm) was attached to the test section (15 mm with thermal conductivity of 0.18 W/[m·K]) to provide uniform heat flux to the surface, starting from the trailing edge of holes to ~15*D* downstream. An insulation sheet (0.02 W/[m·K]) with a thickness of ~10 mm was glued to the back of the plate to reduce the heat loss through the wall. During the test, heat conduction loss was estimated using thermocouple reading and the materials' properties. It was found to be less than 4%. Radiation loss was estimated to be within 9%.

A deliberate calibration was performed to establish the relationship between temperature and emission intensity. The reference condition was set at room temperature. The luminescence intensity (i.e., Eq. (7)) was therefore defined as the ratio of recorded intensity at the reference condition to a certain temperature. Varying the surface temperature of the test model, the TSP was calibrated at various conditions. The results are shown in Fig. 3(a). Further details concerning the TSP calibration process can be found in Ghorbani-Tari et al. [35].

$$T = f\left(\frac{I_{ref}}{I(T)}\right) \tag{7}$$

The TSP experiment had the same spatial resolution as the PSP test. Following the method proposed by Moffat [36], the measurement uncertainty of the local heat transfer coefficient was estimated to be within 10% and the NHFR was estimated to be within 15% based on a 95% confidence level. This uncertainty estimation accounts for various measurement errors, including those regarding voltage, current, heat loss, non-uniform heat flux, and wall temperature.

Before the experiment, a verification study was performed to validate the accuracy of the TSP technique. The heat transfer coefficient of unblown case was well described by the empirical equation (i.e., Eq. (7)) [37] considering an unheated starting length of x_0 with constant heat flux. Fig. 3(b) shows the comparison of the heat transfer coefficients between the measured values by the TSP technique and predictions using the empirical equation. As shown clearly in the figure, the measured heat transfer profile was consistent with the predicted values over the entire measurement of interest. Discrepancies of less than 10% were found between them, which were within the measurement uncertainty. Therefore, the TSP technique is reliable and can be used to measure the temperature on the surface.

$$h_0 = 0.0308\rho c U_\infty \mathrm{Re}^{-0.2}\mathrm{Pr}^{-0.67}\left[1-\left(\frac{x_0}{x_0+x}\right)^{0.9}\right]^{-1/9} \tag{8}$$

3. Results and discussion

3.1. Adiabatic film cooling effectiveness results

The PSP technique was used to quantify the adiabatic effectiveness

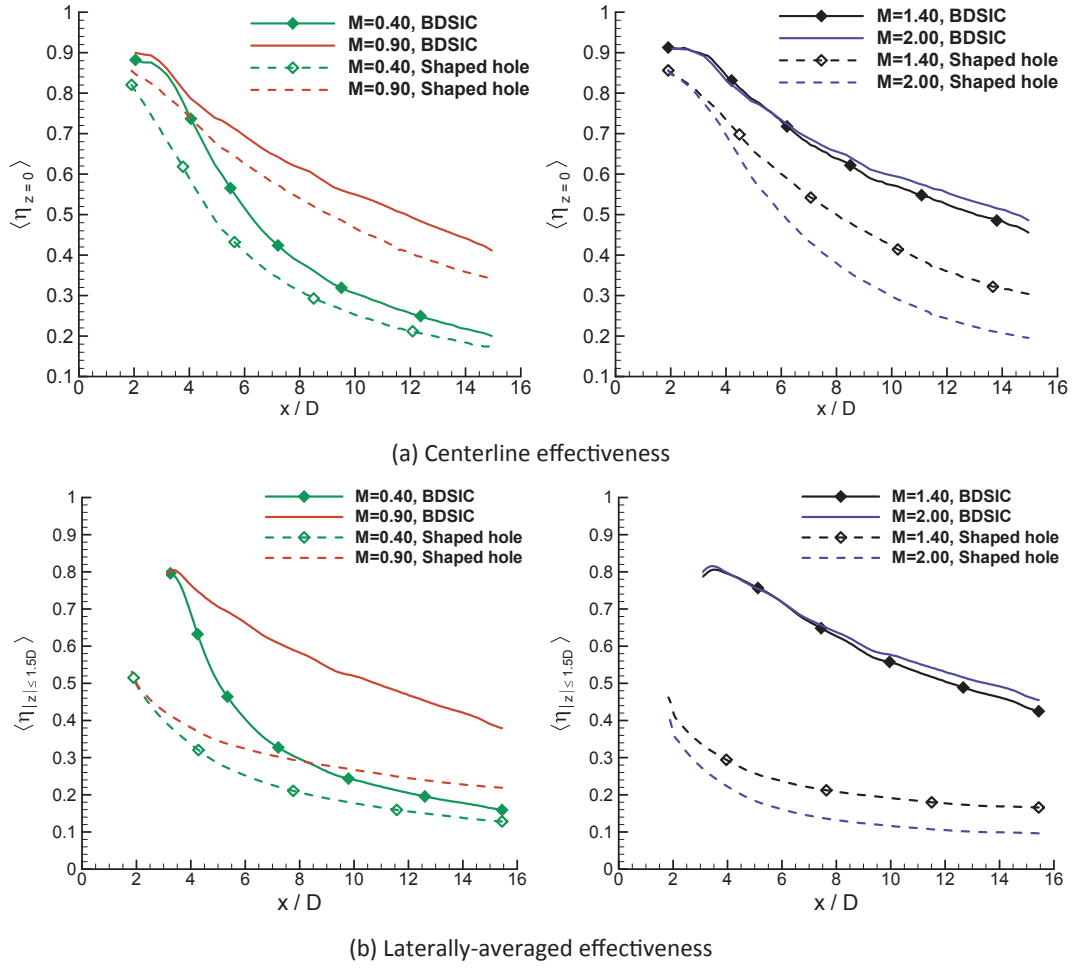

Fig. 5. Comparison of the cooling effectiveness profiles between the shaped hole and BDSIC case at various blowing ratios.

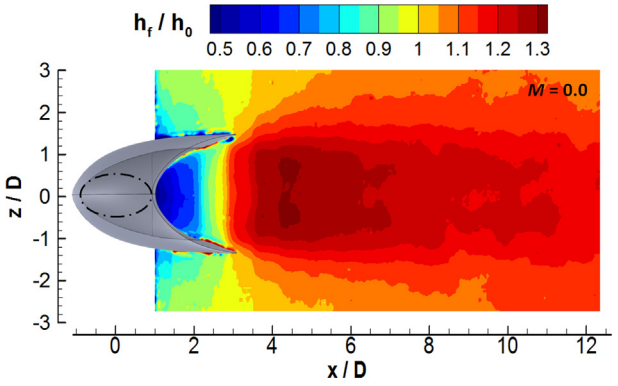

Fig. 6. Measured heat transfer coefficient distribution for the BDSIC designs at zero blowing ratio.

over the surface, which was the first side-by-side comparison between the BDSIC and shaped hole. Measured results could help us further evaluate the potential of the BDSIC concept. Furthermore, the acquired effectiveness results were later correlated with the heat transfer coefficient to derive the high-resolution NHFRs. Note that, previous BDSIC results were reported at a density ratio of 1.5 [1]. But this study used nitrogen as the coolant, rather than carbon dioxide, to ensure equivalent density ratio with that of heat transfer experiments.

Fig. 4 shows the measured effectiveness contours of the BDSIC concept compared to the laidback fan-shaped hole at blowing ratios of $M = 0.40$, 0.90, 1.40, and 2.00. Apparently, the cooling effectiveness of the BDSIC was significantly higher than that of the shaped hole at all blowing ratios. When the blowing ratio was comparative low at $M = 0.40$, although the shaped hole demonstrated a good coolant coverage, the BDSIC showed a greatly improved film coverage behind the dune. As the blowing ratio increased to $M = 0.90$, the footprints behind both cases became wider and longer, indicating augmented effectiveness for shaped and BDSIC holes. However, the phenomenon begins to change as $M > 0.9$. At $M = 1.40$ and 2.00, the regions with high cooling effectiveness (shown in blue) behind the shaped hole became smaller and narrower, indicating the partial takeoff of the high-momentum jet from the test surface. Although the shaped hole was designed to diffuse the coolant jet in both streamwise and spanwise directions, it was unable to hold it as $M > 0.9$. As for the BDSIC, however, it increased monotonically as the blowing ratio increased. This is consistent with the previous conclusion [1]. In general, the dune shell could keep the coolant stream on the surface, leading to significantly better film coverage over the protected surface.

To compare the effectiveness more quantitatively, the centerline and laterally averaged effectiveness curves were computed from the contours and shown in Fig. 5. The centerline effectiveness ($\langle\eta_{z=0}\rangle$) indicates the value along the centerline of the injection holes. The laterally averaged profiles ($\langle\eta_{|z|\leq 1.5D}\rangle$) represent the average quantities of effectiveness along the lateral direction in the region of $-1.5 \leq z/D \leq 1.5$. As shown clearly in Fig. 5, the measured centerline and the laterally averaged effectiveness of the BDSIC were found to be significantly higher than those of the shaped hole. Both exhibited increased effectiveness (including the centerline and laterally averaged profiles) as the blowing ratio increased. But the shaped hole was found

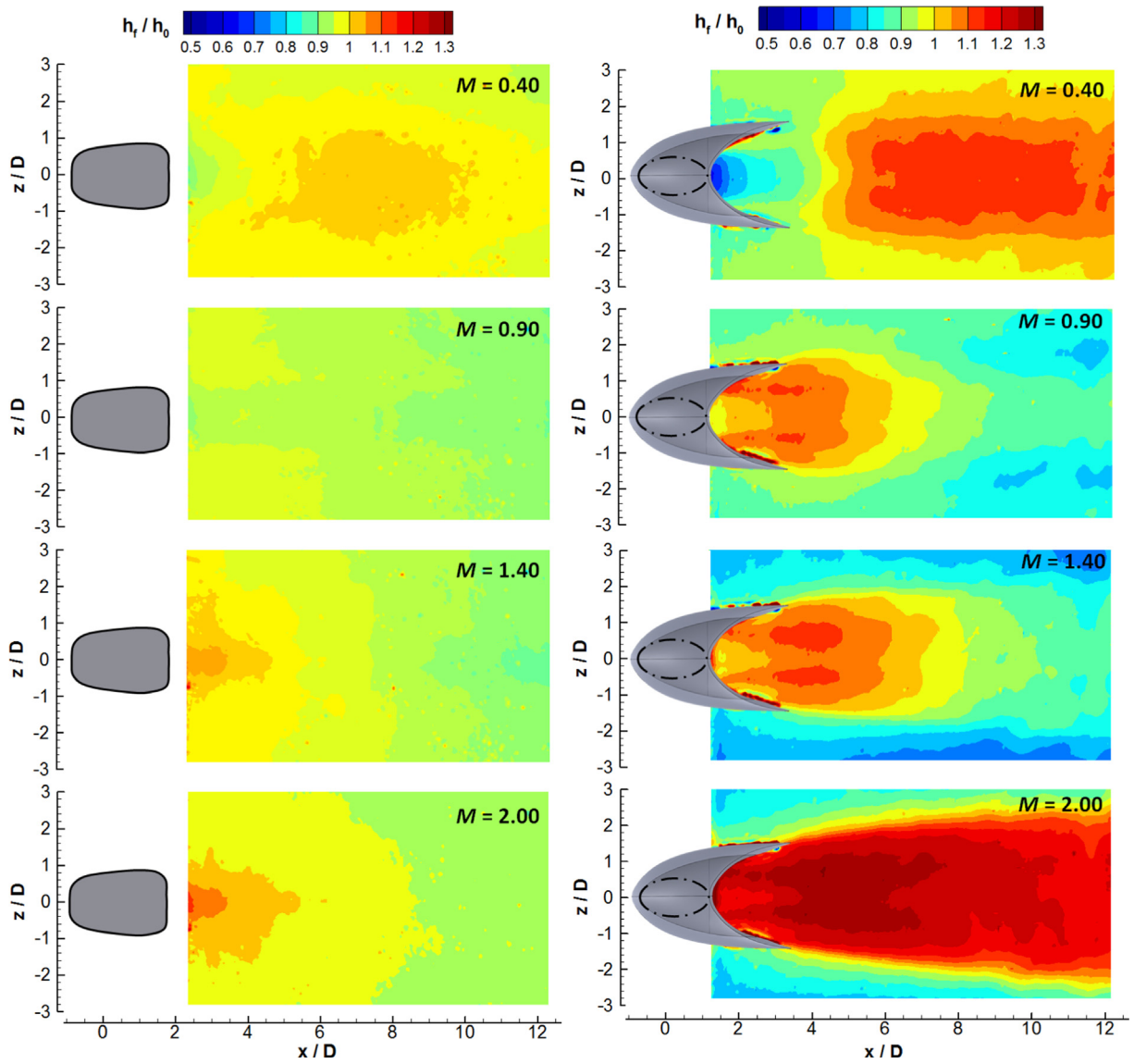

Fig. 7. Measured heat transfer coefficient distributions for the shaped hole and the BDSIC designs at various blowing ratios.

to become smaller as $M > 0.90$. This agrees with the features demonstrated in the spatial contours shown in Fig. 4. Due to the momentum increases, the coolant jet for the shaped hole tended to partially separate from the test plate, leading to deteriorative cooling performance. In contrast, the coolant stream in the BDSIC would be suppressed down by the dune shell and stayed on the surface.

In general, the BDSIC concept demonstrates a greatly augmented cooling effectiveness in comparison to the baseline. More specifically, compared to the shaped hole, improvements of 20–150% in the centerline and 30–400% in the laterally averaged cooling effectiveness were observed behind the BDSIC. Therefore, the BDSIC demonstrate strong potential to provide a wider and more uniform coolant coverage over the protected surface.

3.2. Heat transfer coefficient results

After the PSP test, the original paint was completely removed from the models. The TSP was sprayed on the surface using an airbrush. It was left to dry for 24 h in a clean environment and kept away from dust particles and scratches. Similar experimental setups were used for the TSP experiment, except that the 650-nm band-pass filter was switched to 600 nm. Other configurations, such as camera setting and wind tunnel speed, were kept exactly same to ensure the correlation of the TSP and PSP results.

Fig. 6 shows the heat transfer coefficient contour behind the BDSIC at zero blowing ratio, where h_f is the measured result with film cooling and h_0 is the heat transfer result without film cooling (i.e., heat transfer along the flat plate). It is worth mentioning that as a small variation was observed between the flat plate and shaped hole at $M = 0$, only the heat transfer map of the BDSIC is shown here for conciseness. Clearly, Fig. 6 shows the effect of the dune shape on the heat transfer performance downstream of the BDSIC concept. As expected, the appearance of the Barchan dune on the surface generated a strong turbulent wake that greatly promoted heat transfer (shown in red) within the mainstream and surface wall. The affected region was found to start right after the dune's horn and continue all the way downstream to $x/D = 12$. Furthermore, its effect spread so widely in the lateral direction that the heat transfer coefficient was found to be ~10% higher than the flat plate at the lateral $z/D = \pm 3$ position. Along the streamwise direction, a maximum enhancement of the heat transfer coefficient of ~30% was observed at $x/D = 4.5$, which is believed to be the flow reattachment location [38]. It can also be seen that a significantly low heat transfer region (shown in blue) was spotted in the bay of the dune shell (i.e., $1.0 < x/D < 2.5$). Due to the arched shape of Barchan dune, it created

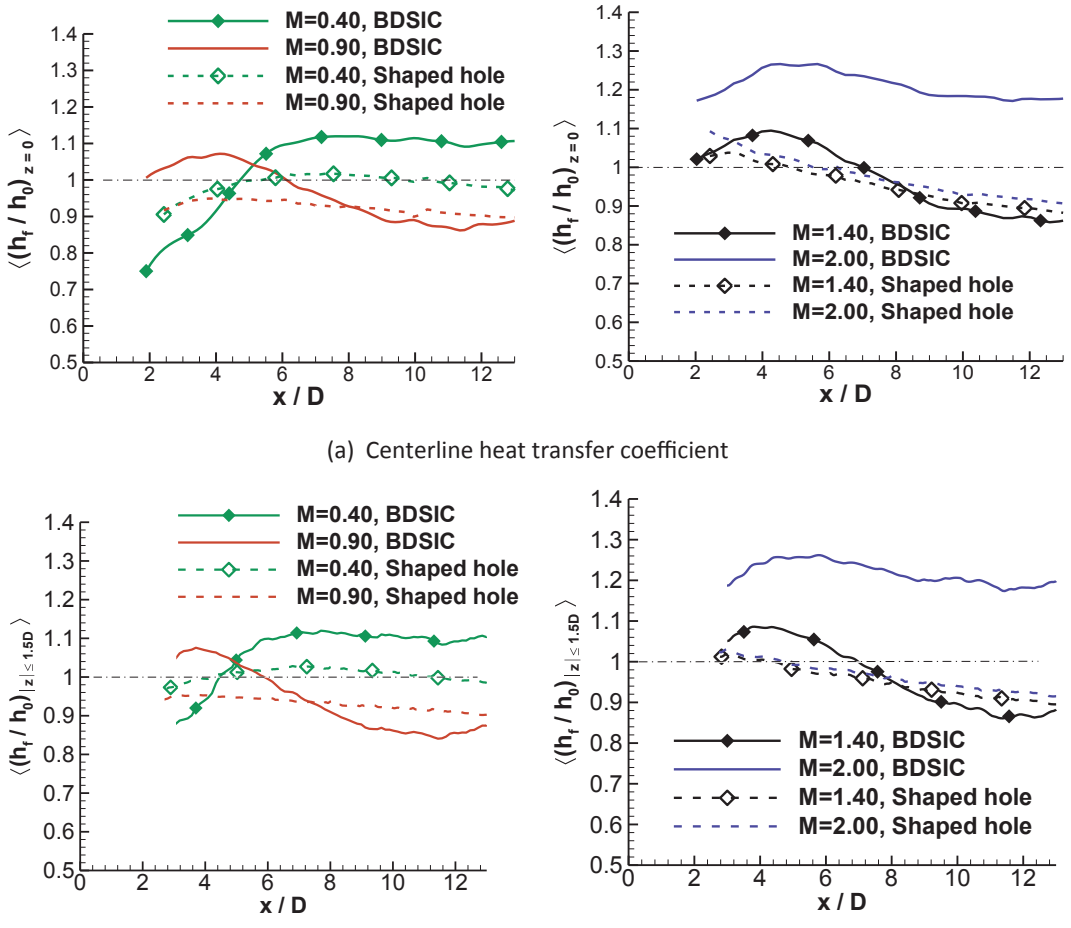

Fig. 8. Comparison of the heat transfer coefficient profiles between the shaped hole and BDSIC cases at various blowing ratios.

an almost "dead zone," leading to dramatically decreased heat transfer performance.

Figs. 7 and 8 show the comparison of the measured heat transfer coefficients between the shaped and BDSIC holes at blowing ratios of $M = 0.40$, 0.90, 1.40, and 2.00. As shown in the figures, the heat transfer coefficients, h_f/h_0, behind the shaped hole were typically found to be typically around 1, indicating a similar magnitude of heat transfer with that of the unblown case (i.e., without film cooling). But the BDSIC configuration showed dramatically different distributions that the region with high heat transfer was found to vary as the blowing ratio increased. In general, the BDSIC design demonstrated an augmented heat transfer coefficient, h_f/h_0, compared to the shaped hole for most of the test cases.

At $M = 0.40$, the heat transfer coefficient (i.e., ~0.9) around the exit of the shaped hole was slightly lower than that of the unblown case. As the coolant discharged from the hole, it would cover the surface that thickened the boundary layer thickness and decreased the heat transfer rate. But the heat transfer gradually rose up as the coolant moved further downstream to $x/D = 8$. The attached coolant became chaotic due to the intensive turbulent mixing within flows, which can be seen clearly from the centerline and laterally averaged h_f/h_0. Increasing the blowing ratio to $M = 0.90$, the region with low heat transfer became larger for the shaped hole, starting from the hole exit to all the way across the measurement of interest. Recall that the film effectiveness at $M = 0.90$ was the highest among all the test cases for the shaped hole, as shown in Figs. 4 and 5. This indicates uniform coverage of coolant film behind the hole. Furthermore, the coolant jet velocity was close to the mainstream flow (i.e., $VR = 0.9$), which largely reduced the shear stress, thereby mitigating the turbulent mixing between the coolant and mainstream flow. All these factors led to the decreased centerline and laterally averaged h_f/h_0 at $M = 0.90$ in comparison to the $M = 0.40$ case.

Further increased blowing ratio to $M = 1.40$ and 2.00, the high-momentum jet of shaped hole partially separated from the surface, as shown in Fig. 4, leading to intensive interactions within the coolant and in the mainstream at the exit of the shaped hole. This is the reason why the heat transfer coefficient around the hole exit region was moderately higher than that of the lower M cases. As shown quantitatively in Fig. 8, the centerline and laterally averaged h_f/h_0 was found to decrease from ~1.0 at $x/D = 4$ to ~0.9 at $x/D = 12$. This may have been caused by the coolant accumulation in the downstream region. It also can be seen that the improvement in the h_f/h_0 was quite small as the blowing ratio increased from $M = 1.40$ to $M = 2.00$, indicating the approaching limit of the heat transfer coefficient for the shaped hole.

A completely different phenomenon was observed for the BDSIC cases. At $M = 0$, the turbulent wake generated by the dune shape greatly promoted the heat transfer between the mainstream and protected surface, as shown in Fig. 6. However, at $M = 0.40$, the region with high heat transfer became much smaller. As coolant injected from the BDSIC, it largely reduced the size of the wake region and alleviated the flow interaction within the dune and mainstream, which led to a reduced heat transfer process. Increasing the blowing ratio to $M = 0.90$, the turbulent wake was further reduced. The previous region with a high heat transfer coefficient (i.e., at $M = 0.40$) disappeared completely and another region showed up right behind the dune. The detailed centerline and laterally averaged h_f/h_0 clearly showed the trend:

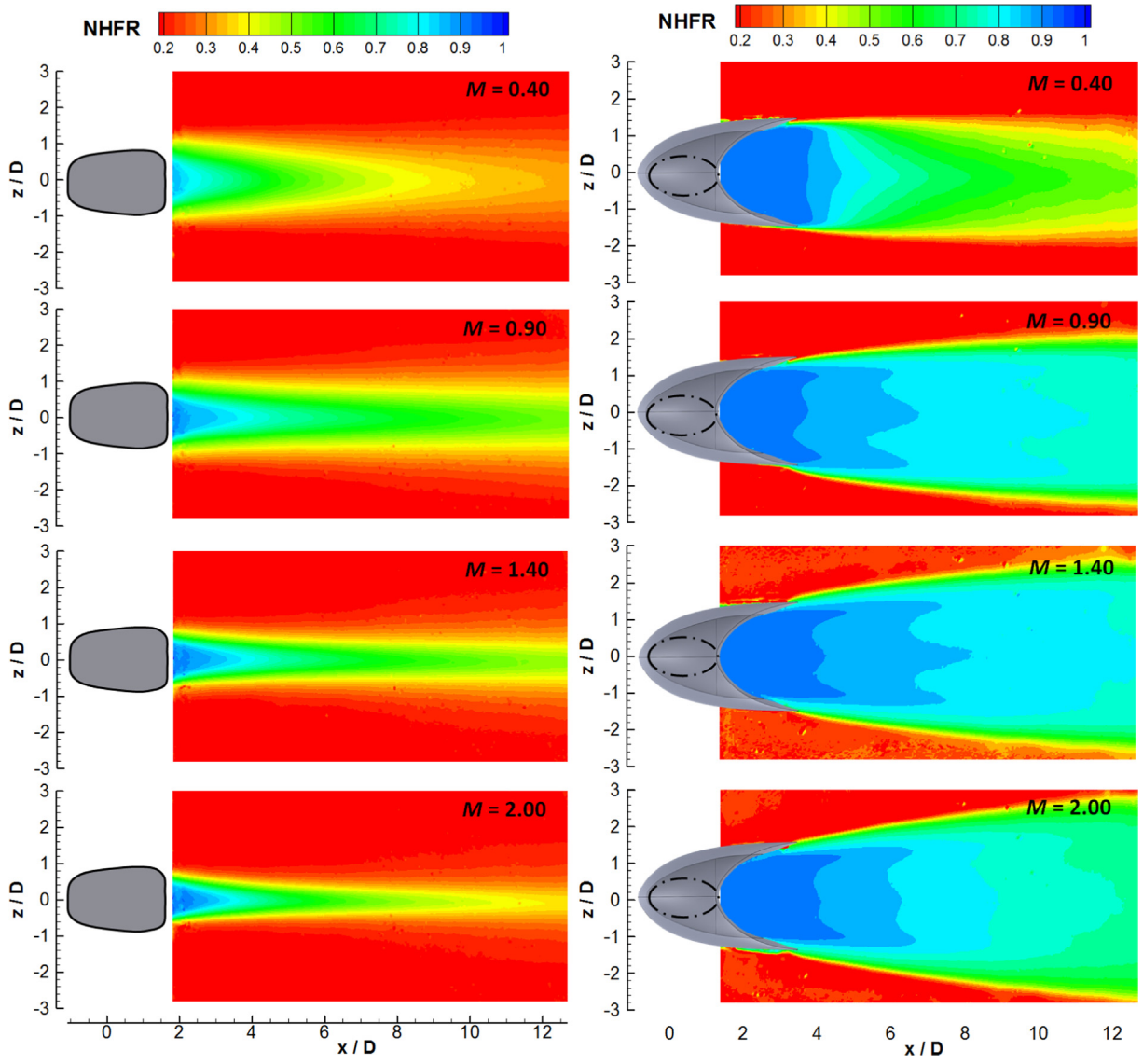

Fig. 9. Net heat flux reduction maps for the shaped hole and the BDSIC designs at various blowing ratios.

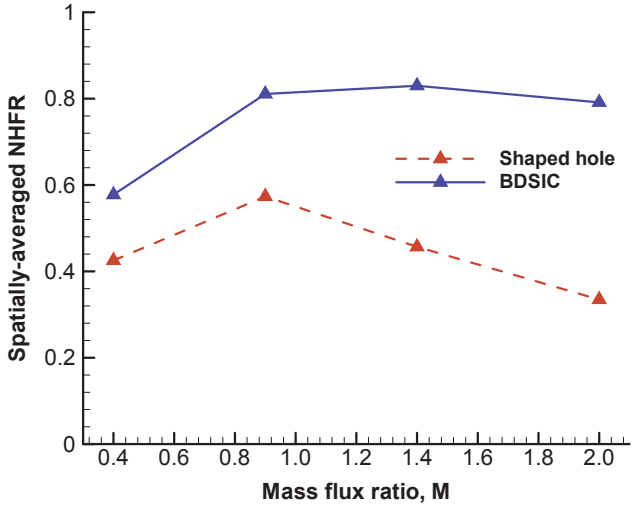

Fig. 10. Spatially-averaged NHFR for the shaped hole and the BDSIC designs at various blowing ratios.

compared to the BDSIC at $M = 0.40$, although a peak appeared at $x/D = 4$ for $M = 0.90$, the downstream region exhibited a large decrease at $x/D = 11$, an approximately 25% decrease in the centerline and laterally averaged h_f/h_0. With a further increased blowing ratio of $M = 1.40$, a very similar pattern was observed for the $M = 0.90$ case behind the BDSIC, except for the slight increase in h_f/h_0 near the dune region. But when $M = 2.00$, the heat transfer coefficient increased significantly. Since the injecting velocity (i.e., $VR = 2.04$) is much higher than that of ambient flow, the rebounded high-momentum jet would generate intensive flow interactions, thus led to enhanced heat transfer coefficient behind the BDSIC.

Compared to the shaped hole, the centerline and laterally averaged h_f/h_0 (shown in Fig. 8) for the BDSIC configuration was initially higher than the shaped hole at $M = 0.40$, which was mainly due to the dune geometry effect above the wall. As the blowing ratio increased to $M = 0.90$ and 1.40, the injected coolant alleviated the flow separation and lowered the h_f/h_0 in the downstream region of the BDSIC. But, a significantly higher h_f/h_0 was observed for the BDSIC case at $M = 2.00$, approximately 25% higher than that of the shaped hole. This indicates that more heat for the BDSIC could be transferred from the hot gas to the protected surface at $M = 2.00$.

3.3. Net heat flux reduction analysis

To evaluate the overall cooling performance of the BDSIC holes, the NHFR was estimated based on the adiabatic effectiveness and heat transfer coefficient distributions (shown in Fig. 9). Red represents a region with small heat flux reduction, a potential high-temperature region, while the blue indicates large heat flux reduction, a potential low-temperature region. As shown clearly in Fig. 9, the footprint of the NHFR for the shaped hole was found to first become wider and longer as M increased from 0.40 to 0.90, but it then decreased as M further increased to 1.40 and 2.00. This demonstrated similar effectiveness distributions to those of the shaped hole. As for the BDSIC, its footprint increased monotonically as M varied from 0.40 to 1.40, but a slightly decreased NHFR map was observed at $M = 2.00$. This was caused by the increasing turbulent flow mixing within the coolant and mainstream, as shown in Fig. 7.

Finally, spatially averaged NHFR was evaluated to compare the overall cooling performance of the different test cases. It was defined as $\frac{1}{A}\iint NHFR_{xz}\,dA$, where A is the area of interest (i.e., $2 \le x/D \le 13$ and $-1.5 \le z/D \le 1.5$) and $NHFR_{xz}$ is the corresponding heat reduction at each location. As shown clearly in Fig. 10, the spatially averaged NHFR of the shaped hole reached a maximum value of ~60% at $M = 0.90$ but then dropped rapidly as $M > 0.90$. This is believed to be related to the jet lift-off event for the shaped hole. A similar trend was observed for the BDSIC, increasing rapidly at first but then reaching a relatively stable value at ~80%. It is worth noting that as $M > 1.40$, the enhanced turbulent mixing behind the BDSIC made the spatially averaged NHFR decrease gradually. Compared to the shaped hole, although the heat transfer coefficient, h_f/h_0, behind the BDSIC was approximately 10–20% higher, the measured values still showed an augmentation of 50–150% in mean NHFR due to the significantly improved effectiveness distribution in comparison to the shaped hole.

4. Conclusion

An experiment was conducted to evaluate the cooling performance of BDSIC concept to further determine its suitability for engine cooling. Adiabatic film effectiveness, heat transfer coefficient, and NHFR were quantified separately in comparison to the shaped hole. Adiabatic effectiveness was measured by PSP technique and the heat transfer coefficient was obtained using the TSP technique. During the test, either N_2 or air was discharged from an injection hole at an inclination angle of 35°. The effect of the blowing ratio (i.e., $M = 0.40$, 0.90, 1.40, and 2.00) on film cooling's surface quantities was examined in a comprehensive manner based on the quantitative PSP and TSP results.

The PSP results clearly revealed that the measured cooling effectiveness behind the BDSIC concept was significantly higher than the shaped hole for all blowing ratios. At relatively low blowing ratios of $M = 0.40$ and 0.90, the coolant jet in the shaped hole was confirmed to attach well on the surface and demonstrated increased effectiveness distributions. However, it lifted off partially as $M > 0.9$ due to the increased momentum of the coolant jet. As for the BDSIC configuration, the dune shell could hold the coolant on the surface, leading to significantly higher film effectiveness over the protected surface. More specifically, improvements of 20–150% in the centerline and 30–400% in the laterally averaged cooling effectiveness were observed behind the BDSIC compared to the shaped hole.

As expected, the TSP results revealed that the appearance of the dune shape greatly promoted the heat transfer from the mainstream to the surface, but it started to decrease as $M > 0$ since coolant injection alleviated the flow separation. During the experiment, the heat transfer coefficients behind the shaped hole were typically around one, indicating a similar magnitude of heat transfer with the unblown case. Nevertheless, the BDSIC configuration exhibited a dramatically different pattern. Specifically, the region with high heat transfer varied as M increased. In general, the BDSIC demonstrated a higher heat transfer coefficient, h_f/h_0, than the shaped hole at relatively high values of M. For example, there was an augmentation of ~25% for the BDSIC compared to the shaped hole.

Due to the jet lift-off event, the spatially averaged NHFR of the shaped hole reached a maximum at $M = 0.90$, but then decreased rapidly as $M > 0.90$. A similar trend was observed for the BDSIC, which first increased rapidly but then reached a relatively stable value at ~80%. Compared to the shaped hole, although the heat transfer coefficient, h_f/h_0, behind the BDSIC was approximately 10–20% higher, the measured mean NHFR still showed an improvement of 50–150% for the BDSIC case.

It is worth noting that though the measured results clearly demonstrate that the BDSIC can greatly improve the overall film cooling performance, extensive investigations are still needed to further inspect the relevant parameters, such as the compressibility effect, density effect, turbulent intensity effect, and discharge coefficient.

Acknowledgments

The authors gratefully acknowledge the financial support for this study from the National Natural Science Foundation of China (11725209, 51806138) and the Shanghai Sailing Program (18YF1411300).

References

[1] W. Zhou, H. Hu, A novel sand-dune-inspired design for improved film cooling performance, Int. J. Heat Mass Transf. 110 (2017) 908–920, https://doi.org/10.1016/j.ijheatmasstransfer.2017.03.091.
[2] D.G. Bogard, K.A. Thole, Gas turbine film cooling, J. Propuls. Power 22 (2006) 249–270, https://doi.org/10.2514/1.18034.
[3] R.S. Bunker, A review of shaped hole turbine film-cooling technology, J. Heat Transfer. 127 (2005) 441, https://doi.org/10.1115/1.1860562.
[4] W. Zhou, B. Johnson, H. Hu, Effects of flow compressibility and density ratio on film cooling performance, J. Propuls. Power 33 (2017) 964–974, https://doi.org/10.2514/1.B36275.
[5] R.J. Goldstein, E.R.G. Eckert, F. Burggraf, Effects of hole geometry and density on three-dimensional film cooling, Int. J. Heat Mass Transf. 17 (1974) 595–607, https://doi.org/10.1016/0017-9310(74)90007-6.
[6] R.S. Bunker, Film cooling effectiveness due to discrete holes within a transverse surface slot, Turbo Expo 2002, Parts A B, vol. 3, ASME, 2002, pp. 129–138, , https://doi.org/10.1115/GT2002-30178.
[7] Y. Lu, D. Faucheaux, S.V. Ekkad, Film cooling measurements for novel hole configurations, ASME 2005 Summer Heat Transf. Conf. Collocated with ASME 2005 Pacific Rim Tech. Conf. Exhib. Integr. Packag. MEMS, NEMS, Electron. Syst. ASME, 2005, pp. 59–66, , https://doi.org/10.1115/HT2005-72396.
[8] J. Han, S. Dutta, S. Ekkad, Gas Turbine Heat Transfer and Cooling Technology, second ed., CRC Press, New York, 2012.
[9] J.D. Heidmann, S. Ekkad, A novel antivortex turbine film-cooling hole concept, J. Turbomach. 130 (2008) 031020, https://doi.org/10.1115/1.2777194.
[10] A. Dhungel, Y. Lu, W. Phillips, S.V. Ekkad, J. Heidmann, Film cooling from a row of holes supplemented with antivortex holes, J. Turbomach. 131 (2009) 021007, https://doi.org/10.1115/1.2950059.
[11] J.S. Liu, M.F. Malak, L.A. Tapia, D.C. Crites, D. Ramachandran, B. Srinivasan, G. Muthiah, J. Venkataramanan, Enhanced film cooling effectiveness with new shaped holes, Heat Transf. Parts A B, vol. 4, ASME, 2010, pp. 1517–1527, , https://doi.org/10.1115/GT2010-22774.
[12] M.A. Hossain, R. Prenter, R.K. Lundgreen, A. Ameri, J.W. Gregory, J.P. Bons, Experimental and numerical investigation of sweeping jet film cooling, J. Turbomach. 140 (2017) 031009, https://doi.org/10.1115/1.4038690.
[13] W. Zhou, H. Hu, Improvements of film cooling effectiveness by using Barchan dune shaped ramps, Int. J. Heat Mass Transf. 103 (2016) 442–456, https://doi.org/10.1016/j.ijheatmasstransfer.2016.07.066.
[14] R.J. Vedula, D.E. Metzger, A method for the simultaneous determination of local effectiveness and heat transfer distributions in three-temperature convection situations, in: Int. Gas Turbine Aeroengine Congr. Expo. 36th, Orlando, FL, June 3–6, 1991, ASME, 1991, 9 P. < http://adsabs.harvard.edu/abs/1991gatu.confR....V > (accessed March 21, 2018).
[15] S. Baldauf, A. Schulz, S. Wittig, High-resolution measurements of local effectiveness from discrete hole film cooling, J. Turbomach. 123 (2001) 758, https://doi.org/10.1115/1.1371778.
[16] B. Johnson, W. Tian, K. Zhang, H. Hu, An experimental study of density ratio effects on the film cooling injection from discrete holes by using PIV and PSP techniques, Int. J. Heat Mass Transf. 76 (2014) 337–349, https://doi.org/10.1016/j.ijheatmasstransfer.2014.04.028.
[17] D.P. Narzary, K.-C. Liu, J.-C. Han, Influence of coolant density on turbine blade platform film-cooling, J. Therm. Sci. Eng. Appl. 4 (2012) 021002, , https://doi.org/10.1115/1.4005732.

[18] S. Baldauf, A. Schulz, S. Wittig, High-resolution measurements of local heat transfer coefficients from discrete hole film cooling, J. Turbomach. 123 (2001) 749, https://doi.org/10.1115/1.1387245.
[19] R.A. Russin, D. Alfred, L.M. Wright, Measurement of detailed heat transfer coefficient and film cooling effectiveness distributions using PSP and TSP, Heat Transf. Parts A B, vol. 3, ASME, 2009, pp. 807–817, , https://doi.org/10.1115/GT2009-59975.
[20] P.H. Chen, R.J. Goldstein, Convective transport phenomena on the suction surface of a turbine blade including the influence of secondary flows near the endwall, J. Turbomach. 114 (1992) 776, https://doi.org/10.1115/1.2928031.
[21] M. Häring, A. Bölcs, S.P. Harasgama, J. Richter, Heat transfer measurements on turbine airfoils using the naphthalene sublimation technique, J. Turbomach. 117 (1995) 432, https://doi.org/10.1115/1.2835679.
[22] L.M. Wright, S.T. McClain, M.D. Clemenson, Effect of density ratio on flat plate film cooling with shaped holes using PSP, J. Turbomach. 133 (2011) 041011, https://doi.org/10.1115/1.4002988.
[23] A. Khojasteh, S. Wang, D. Peng, S. Yavuzkurt, Y.Z. Liu, Structure analysis of adiabatic film cooling effectiveness in the near field of a single inclined jet: measurement using fast-response pressure-sensitive paint, Int. J. Heat Mass Transf. 110 (2017) 629–642, https://doi.org/10.1016/J.IJHEATMASSTRANSFER.2017.03.069.
[24] R. Schroeder, K. Thole, Adiabatic effectiveness measurements for a baseline shaped film cooling hole, ASME Turbo Expo 2014, GT2014-25992, 2014, pp. 1–13, , https://doi.org/10.1115/GT2014-25992.
[25] H.D. Ammari, N. Hay, D. Lampard, Simulation of cooling film density ratios in a mass transfer technique, p. V004T08A025, Heat Transf. Electr. Power; Ind. Cogener. vol. 4, ASME, 1989, , https://doi.org/10.1115/89-GT-200.
[26] J.N. Shadid, E.R.G. Eckert, The mass transfer analogy to heat transfer in fluids with temperature-dependent properties, J. Turbomach. 113 (1991) 27, https://doi.org/10.1115/1.2927734.
[27] D. Charbonnier, P. Ott, M. Jonsson, F. Cottier, T. Köbke, Experimental and numerical study of the thermal performance of a film cooled turbine platform, ASME Turbo Expo 2009, vol. 3, Pts A B, ASME, 2009, , https://doi.org/10.1115/GT2009-60306.
[28] V.L. Eriksen, R.J. Goldstein, Heat transfer and film cooling following injection through inclined circular tubes, J. Heat Transfer. 96 (1974) 239, https://doi.org/10.1115/1.3450171.
[29] D.G. Bogard, Airfoil film cooling, Section 4.2.2.1, Gas Turbine Handb. National Energy Technology Laboratory, 2006, http://www.alrc.doe.gov/technologies/coalpower/turbines/refshelf/handbook/4.2.2.1.pdf.
[30] J. Dittmar, A. Schulz, S. Wittig, Adiabatic effectiveness and heat transfer coefficient of shaped film cooling holes on a scaled guide vane pressure side model, Int. J. Rotating Mach. 10 (2004) 345–354, https://doi.org/10.1155/S1023621X04000351.
[31] M. Gritsch, S. Baldauf, M. Martiny, A. Schulz, S. Wittig, The superposition approach to local heat transfer coefficients in high density ratio film cooling flows, p. V003T01A048, Heat Transf. Electr. Power; Ind. Cogener. vol. 3, ASME, 1999, , https://doi.org/10.1115/99-GT-168.
[32] R. Johnson, J. Maikell, D. Bogard, J. Piggush, A. Kohli, M. Blair, Experimental study of the effects of an oscillating approach flow on overall cooling performance of a simulated turbine blade leading edge, Heat Transf. Parts A B, vol. 3, ASME, 2009, pp. 1009–1016, , https://doi.org/10.1115/GT2009-60290.
[33] A.K. Sinha, D.G. Bogard, M.E. Crawford, Film-cooling effectiveness downstream of a single row of holes with variable density ratio, J. Turbomach. 113 (1991) 442, https://doi.org/10.1115/1.2927894.
[34] L.M. Wright, Z. Gao, T.A. Varvel, J.-C. Han, Assessment of steady state PSP, TSP, and IR measurement techniques for flat plate film cooling, Heat Transf. vol. 3, ASME, 2005, pp. 37–46, , https://doi.org/10.1115/HT2005-72363.
[35] Z. Ghorbani-Tari, Y. Chen, Y. Liu, End-wall heat transfer of a rectangular bluff body at different heights: temperature-sensitive paint measurement and computational fluid dynamics, Appl. Therm. Eng. 122 (2017) 697–705, https://doi.org/10.1016/J.APPLTHERMALENG.2017.05.040.
[36] R.J. Moffat, Describing the uncertainties in experimental results, Exp. Therm. Fluid Sci. 1 (1988) 3–17, https://doi.org/10.1016/0894-1777(88)90043-X.
[37] T.L. Bergman, A.S. Lavine, F.P. Incropera, D.P. DeWitt, Fundamentals of heat and mass transfer, Wiley, 2011. < https://www.wiley.com/en-us/Fundamentals+of+Heat+and+Mass+Transfer%2C+7th+Edition-p-9780470501979 > (accessed March 17, 2018).
[38] J.A. Palmer, R. Mejia-Alvarez, J.L. Best, K.T. Christensen, Particle-image velocimetry measurements of flow over interacting barchan dunes, Exp. Fluids. 52 (2011) 809–829, https://doi.org/10.1007/s00348-011-1104-4.